Spectral near-field thermal emission extraction by optical waveguides

Jiayu Li,[1] Jeffrey Wuenschell,[2] Youngseok Jee,[2] Paul R. Ohodnicki,[2,*] and Sheng Shen[1,†]
[1]*Department of Mechanical Engineering, Carnegie Mellon University, Pittsburgh, Pennsylvania 15213, United States*
[2]*United States Department of Energy, National Energy Technology Laboratory, 626 Cochrans Mill Road, Pittsburgh, Pennsylvania 15236, United States*

(Received 9 May 2019; published 12 June 2019)

As far-field thermal emission is limited by blackbody radiation, the significant enhancement of thermal radiation in the near-field plays a vital role in a variety of applications such as infrared sensing, radiation cooling, and thermophotovoltaics. Yet the techniques of exporting the near-field signal to the far field are still not mature, typically relying on complex instrumentation capable of being applied only to the surfaces of model systems and structures. Here we develop an efficient method of extracting near-field thermal radiation to the far field by integrating a nanoscale thermal emitter with a high-index optical waveguide. By directly depositing the emitter onto the optical waveguide, it requires no vacuum gap and enables efficient coupling of near-field thermal radiation into propagating wave-guided modes. A single-mode planar waveguide incorporated with an indium-tin oxide (ITO) film as a thermal emitter is theoretically investigated to prove the feasibility of thermal extraction. The Wiener-chaos expansion method is applied to directly calculate the thermal radiation from the emitter-waveguide system. We experimentally demonstrate the fidelity of the optical-waveguide-assisted near-field thermal extraction by measuring the emission spectrum of an ITO-coated optical fiber and comparing with theoretical predictions. Our experimental demonstration in conjunction with the direct simulation paves the way for effectively extracting near-field thermal radiation with applications in chemical sensing, infrared imaging, and near-field thermal energy management.

DOI: 10.1103/PhysRevB.99.235414

I. INTRODUCTION

Thermal radiation plays an increasingly important role in many applications such as radiative cooling [1,2], gas sensing [3], and thermal management [4,5]. Although technology development for the spectral and directional control of thermal radiation has become more and more sophisticated in recent years [6–11], the intensity of the thermal radiation in the far field is still tightly confined by the blackbody radiation limit. To address this challenge, significant efforts have been taken to utilize the near-field thermal radiation where the energy density of electromagnetic waves can be orders of magnitude larger than that in the far field due to the contribution from evanescent waves [12–22]. However, since near-field thermal radiation is essentially evanescent and eventually decays in the far field [13], there remains a technological challenge for bridging the gap between near-field and far-field thermal radiation.

The existing techniques for measuring the spectral near-field thermal responses are mainly based on near-field scanning optical microscope type experiments, such as the thermal radiation scanning tunneling microscope (TRSTM) [23] or thermal infrared near-field spectroscopy (TINS) [24], where a sharp tungsten tip or platinum-coated atomic force microscope tip is used as a scattering site to couple near-field emission to the far field. The tip-scattered thermal emission is then collected by a Cassegrain-type reflective objective and guided to a Fourier transform infrared spectrometer. However, since the tip-scattered light is so weak, and the reflective objective lens can only catch the light from a very narrow solid angle, both TRSTM and TINS suffer from a low signal-to-noise ratio and thus a low accuracy.

Here, we develop a waveguide coupled thermal emission extraction technique for efficiently extracting near-field thermal radiation to the far field and probing the near-field spectrum of a thin film. The key principle of thermal emission extraction [25] is to convert and guide near-field thermal radiation to the far field through specially designed thermal extractors [16,26,27]. Specifically, some of the electromagnetic modes that are originally evanescent around the interface of the emitter and the emitting ambience can be converted into propagating modes inside the thermal extractors and transported to the far field [28]. Such thermal extractors usually have a larger effective refractive index compared to the emitter and therefore can accommodate more electromagnetic modes. In this work, we employ high-index optical waveguides, such as multimode fibers and single-mode planar waveguides, to demonstrate the near-field thermal emission extraction from a thin indium tin oxide (ITO) film doped with hydrogen (H_2).

II. DIRECT CALCULATION OF THE THERMAL EMISSION EXTRACTION WITH PLANAR WAVEGUIDES

To theoretically elucidate the concept of waveguide coupled thermal extraction, we use ITO as a thermal emitting material and couple it with a single-mode planar waveguide

*paul.ohodnicki@netl.doe.gov
†sshen1@cmu.edu

 ©2019 American Physical Society

as the thermal extractor for the sake of simplicity. Here, we choose ITO as the thermal emitting material because of the good compatibility of ITO thin films with various optical components [29]. Also, the electrical conductivity of the ITO thin films can be tuned via doping to support surface plasmons at both ITO-air and ITO-waveguide interfaces. Based on the optical properties of ITO thin films, their corresponding surface plasmon resonance usually occurs in the near-infrared (NIR) range. The optical properties of ITO thin films are thermally stable yet subject to change under different chemical environments [28]. For example, the exposure to H_2 gas at high temperatures can affect the free carrier concentration inside the ITO thin film and consequently alter the thin film optical properties.

By choosing the ITO thin film as the thermal emitter, silica-based optical waveguides can be used for the thermal extractor due to their high transparency in the NIR range. To demonstrate the feasibility of achieving thermal extraction with the planar waveguide system, we perform the Wiener-chaos expansion (WCE) [8] simulation of the far-field thermal emission from an ITO thin film. The WCE method is a stochastic electromagnetic wave simulation algorithm which decomposes thermally excited current density into a set of complete and orthogonal current density modes [30]. In calculating the contribution from each current density mode, the total thermal radiation can be obtained. The selection of current density forms depends on the geometry of the thermal emitter. Fast convergence is achievable if an appropriate choice of the current density mode set is made.

As a reference simulation, we first calculate the thermal radiation from a stand-alone ITO thin film which is 2-μm wide and 50-nm thick but infinitely long. After that, we calculate the thermal radiation from the same ITO thin film while coupled with a planar waveguide, as shown in Fig. 1(a). The Drude model is applied to calculate the optical properties of the ITO film, where the ITO film carrier concentration and mobility are directly related to the plasma frequency and the collision frequency, respectively [28,31]. The complex refractive index of the ITO film is plotted in Fig. 1(b). As mentioned in the previous section, the ITO film can support surface plasmon resonance whose frequency is identified by the intersection of the real and the imaginary parts of its refractive index. In the case of a carrier concentration of $4.9 \times 10^{20}\ \mathrm{cm}^{-3}$ and a carrier mobility of $30\ \mathrm{cm}^2\ \mathrm{V}^{-1}\ \mathrm{s}^{-1}$, the surface plasmons along the ITO film fall into the transparent window of the silica-based planar waveguide [28]. We therefore use this set of parameters to characterize the ITO film optical properties in the following simulation. The planar waveguide consists of a perfect-electric-conductor substrate layer, a 0.5-μm thick Si_3N_4 core layer and a 0.5-μm thick SiO_2 cladding layer. In presenting the WCE thermal emission results, we use the form of reduced heat flux $\varphi(\lambda)$. The absolute thermal emission intensity $\phi(T)$ in the unit of $\mathrm{W/m}^2$ can be obtained as $\phi(T) = \int \frac{c}{\lambda^2}\frac{\varphi(\lambda)}{A}\Theta(\lambda, T)d\lambda$, where A is the detector area and $\Theta(\lambda, T)$ is the Planck distribution term. Only the z component of the time-averaged Poynting vector that indicates the waveguide power flow direction is collected in both cases for comparison. In the simulation, a two-dimensional (2D) z-normal optical power monitor is placed 10 μm away from the ITO film in both cases. For the case of the coupled ITO-waveguide, the power monitor only covers the cross section of the core layer as indicated by the white dashed line in Fig. 1(a). For the case of the free-standing ITO film, the length of the 2D z-normal monitor in the y direction is set up to be 80 μm in order to capture the contributions from all significant z-component Poynting vectors (see the Supplemental material [32] for more details). Figure 1(b) shows the Poynting vector in the z direction from the free-standing ITO film in the free space. The blue and the red spots around the white-dashed ITO film line are due to the WCE dipole mode excitation [8]. Figures 1(c) and 1(d) plot the field profiles of the Poynting vector in the y and the z directions for the ITO-waveguide case, where part of the thermal radiation emitted from the ITO thin film directly propagates into the free space. The rest of thermal radiation is coupled into the waveguide and extracted to the far field through the planar waveguide. Since we assume that the ITO film and the planar waveguide are both infinitely long in the x direction, the total thermal emission to the far field can be collected by integrating the normal components of the Poynting vectors for each corresponding monitor area.

In Fig. 1(f), the overall heat flux collected from the ITO-waveguide coupled system is about two times larger than that from a free-standing ITO film. The enhancement of the far field heat flux in the waveguide propagation direction indicates significant thermal extraction from the ITO thin film. If we evaluate the total power in terms of detector area, then such the enhancement corresponds to several orders of magnitude more heat flux due to the small detector area required in the case of the ITO-waveguide coupled system. Around the wavelength of 1.55 μm, the surface plasmon resonance (SPR) is thermally excited at the ITO-air interface. At this resonance frequency, a large number of optical modes with a pure imaginary k vector occur around the ITO-air interface. Since the thickness of the ITO thin film is small, such evanescent modes can tunnel through the thin film and reach the ITO-waveguide interface, where they are converted into the propagating modes in the planar waveguide and therefore result in the second peak in reduced heat flux curves. Provided that the SPR is a near-field effect, the resonance peak is relatively weak in the pure far field case yet much stronger with thermal extraction. It should be noted here that the SPR feature is still observable in the far field for the free-standing ITO film due to the end-excitation mechanism [33]. The small peak around the wavelength of 1.1 μm in the blue curve is due to the Fabry-Pérot cavity resonance formed by the cladding layer and the ITO thin film. Although the planar waveguide system demonstrates the capability of enhancing far field thermal radiation through thermal extraction, it is challenging from an experimental perspective to extend planar waveguides into the far field region at a long distance.

III. EXPERIMENTAL DEMONSTRATION OF THE THERMAL EMISSION EXTRACTION WITH OPTICAL FIBERS

Compared with the planar waveguide in Fig. 1, optical fibers provide a more practical platform to achieve thermal emission extraction. The advantages of using an optical fiber for thermal extraction are twofold. First, optical fibers can be

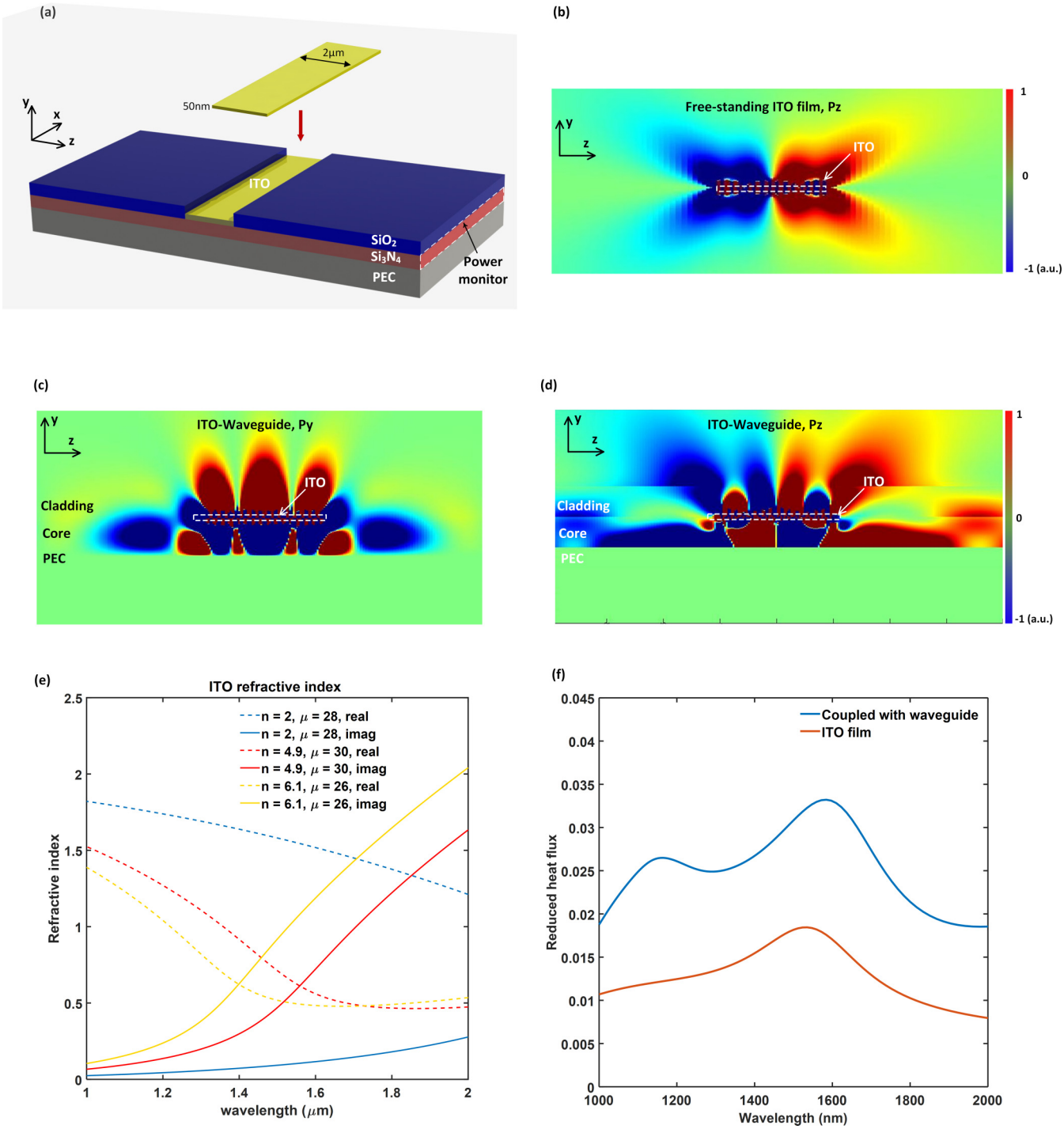

FIG. 1. (a) Schematic of a free-standing ITO thin film compared with the ITO-waveguide system. (b) The z component of the Poynting vector in the y-z plane for the free-standing ITO film. (c) The y component of the Poynting vector in the y-z plane for the ITO-waveguide system. (d) The z component of the Poynting vector in the y-z plane for the ITO-waveguide system. (e) Complex refractive index of an ITO thin film for different carrier concentration (n in the unit of 10^{20} cm^{-3}) and mobility values (μ in the unit of cm^2 V^{-1} s^{-1}). (f) Reduced thermal emission of the free-standing ITO thin film and the ITO-waveguide system.

easily integrated with other optical components or analysis tools like spectrometers. Second, the emitter-fiber system can be easily fabricated in practice. Here, we experimentally measure the thermal emission spectrum of ITO thin films doped by H_2 gas with different concentrations and compare the measurement results with the direct simulations from the WCE method [8].

The thermal emission from an ITO film on the coated optical fiber is measured in a tube furnace reactor system [depicted in Fig. 2(a)], fitted with custom-built end caps to allow a variety of gas mixtures to be flowed across the fiber at elevated temperatures. Thermal emission is collected from one end of the fiber using an optical spectrum analyzer (OSA), which spectrally resolves the collected light from 1.0

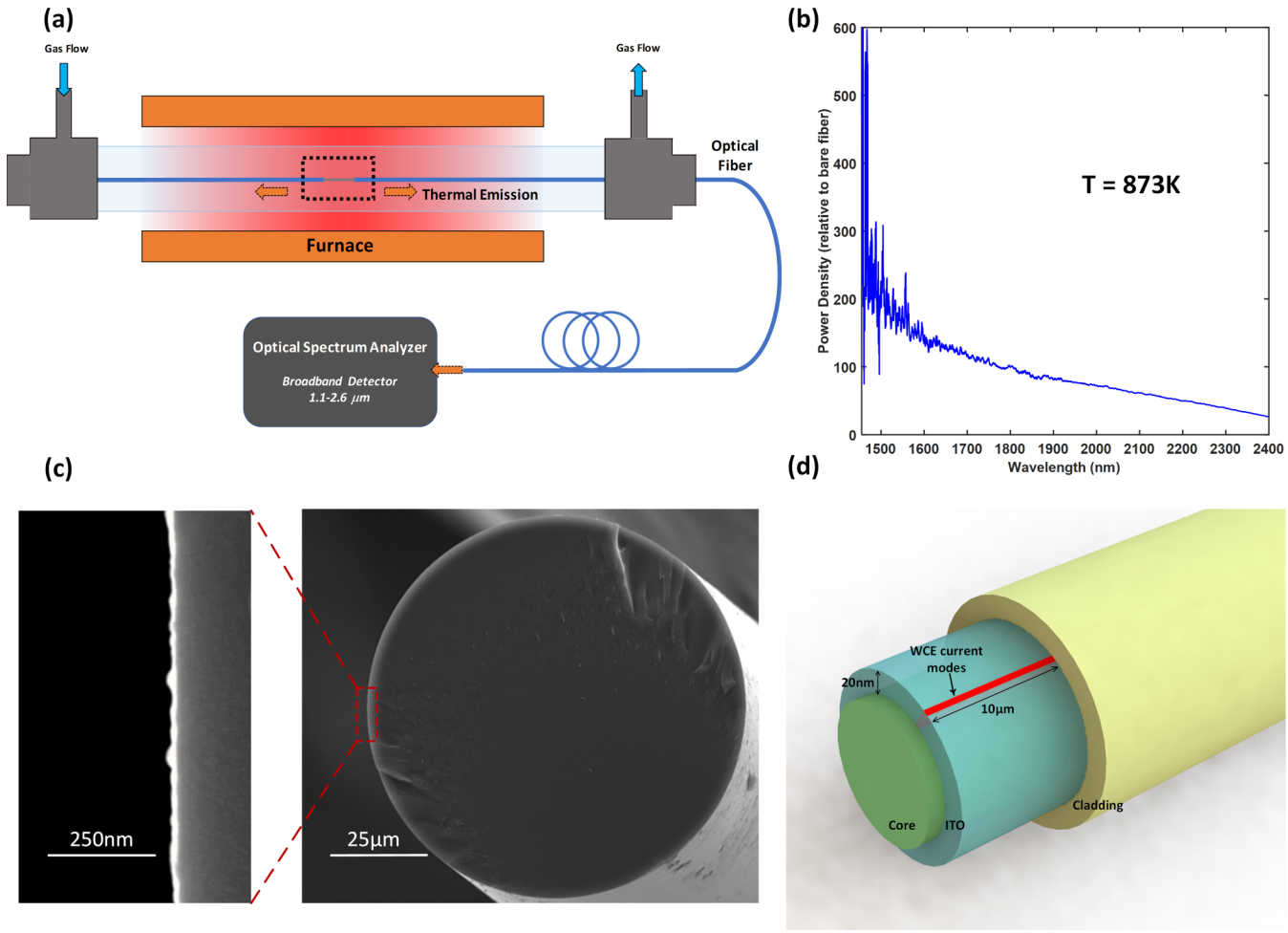

FIG. 2. (a) Schematic of the experimental system, (b) Ratio of the absolute thermal emission intensities for the ITO coated and the uncoated fibers. (c) Schematic of the WCE simulation regime. (d) Scanning electron microscope image of the etched fiber coated with an ITO thin film. Inset: zoomed in image of the ITO-fiber interface.

to 2.6 μm. First, the thermal emission of the fiber sample is collected under ambient atmosphere (no gas flow, open end caps). To verify that the majority of the collected emission power is essentially from the ITO thin film, we also measure the ratio of the absolute emission intensity for the ITO coated and the uncoated fibers. The spectral emission ratio is plotted in Fig. 2(b). Below 1400-nm wavelength, the signal associated with the bare fiber is small and the detector sensitivity is weak and therefore the ratio in that range behaves like a noise term. The overall magnitude of the ratio ranges from $\sim$30 to above 100, which confirms that the thermal emission from the ITO thin film dominates the measured signal in our experimental results.

As shown in Fig. 2(c), the entire thermal extraction system consists of a 20-nm-thick and 3-in-long ITO cylindrical-shape thin film and a 105-μm core optical fiber where the silica cladding is etched. The huge aspect ratio of the ITO thickness and length incurs a heavy computation load for the direct simulation in terms of meshing and calculation time. To tackle this issue, we take the following two steps to mitigate the computation load. First, we take advantage of the continuous rotational symmetry of the ITO thin film layer and only expand the thermal currents within an angle range of 3.8×10^{-4} rad with respect to the center of the fiber core point. Therefore, the dimension of the cross-section simulation area is reduced. Second, we assume that for the ITO layer in the middle part of the whole emitting section, the extracted thermal emission will be balanced by the absorption of the ITO thin film and the fiber core at thermal equilibrium and finally reach a saturation state. Thus, only the ITO thin film in proximity to the intersection region of the etched and the intact fiber portions will significantly contribute to the total thermal extraction signal. In our simulation, a 10-μm long ITO thin film is considered for the WCE mode expansion, as shown in Fig. 2(d).

The total power collected from the 20-nm-thick ITO thin film through the optical fiber is shown in Fig. 3(a), where the power is measured by the OSA as a function of temperature ranging from room temperature to 900 K. The collected thermal emission spectrum as a function of temperature ranging from 473 to 873 K is plotted in Fig. 3(c). The total collected power can be determined by summing the power density/spectral flux (Φ_λ) weighted by the wavelength spread per pixel ($\Delta\lambda_i$), $P_{\text{Total}} = \sum_i \Phi_\lambda(\lambda_i)\Delta\lambda_i$. The WCE simulation results where the carrier concentration of the ITO film is set to be $4.9 \times 10^{20}\,\text{cm}^{-3}$ are plotted in Fig. 3(b). It can be

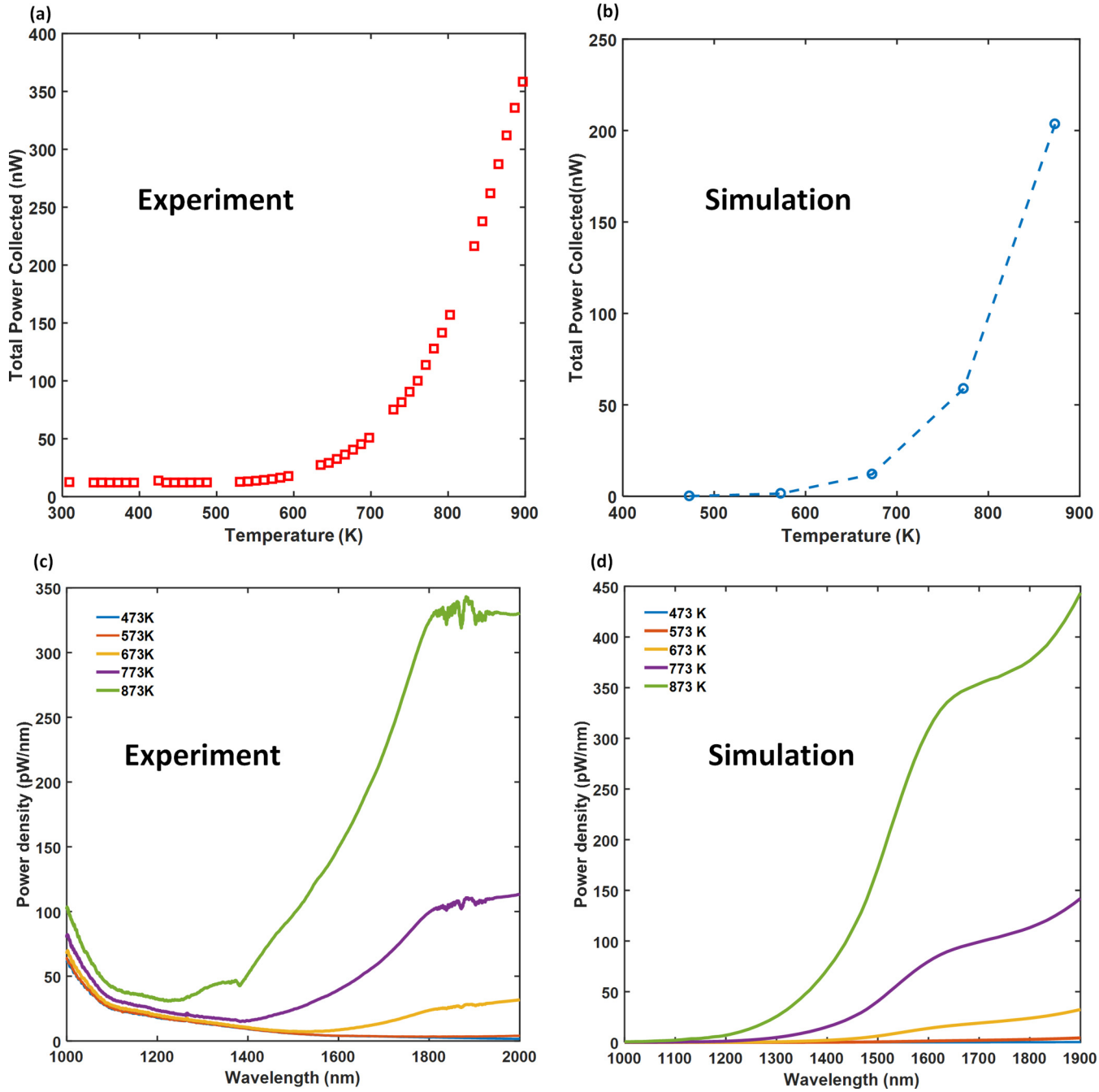

FIG. 3. Total thermal emission power collected from (a) the experiment and (b) the WCE simulation at different temperatures. The corresponding power density spectrum from (c) the experiment and (d) the WCE simulation.

seen that the experimentally measured total power agrees well with the simulation result. In general, the collected power is on the order of nanowatts. A further step of measuring thermal emission spectrum from the ITO thin film is taken to reveal the underlying physics behind the thermal extraction process. In Figs. 3(c) and 3(d), the spectral power densities from experiment and simulation are plotted. As the temperature of the ITO thin film increases, the power density dramatically boosts up, in which a "bump" emerges. The wavelength of the bump is around 1.7 μm, which corresponds to the SPR wavelength of the ITO thin film. The position of the ITO plasmon resonance remains the same for different working temperatures, which indicates that the ITO thin film is of good quality and thermal stability. Since the SPR is, in general, a localized phenomenon and strongly confined at the interface with limited propagation length, the observation of such resonance in the far-field power density spectrum is indeed a consequence of thermal extraction. As the plasmon modes are excited at the ITO-air interface, they can tunnel through the thin film into the interface between the ITO film and the fiber. Because the fiber can accommodate more optical modes in the k space, those plasmon modes that are originally evanescent in the air now become propagating modes in the fiber. Through the mode coupling at the ITO-fiber interface,

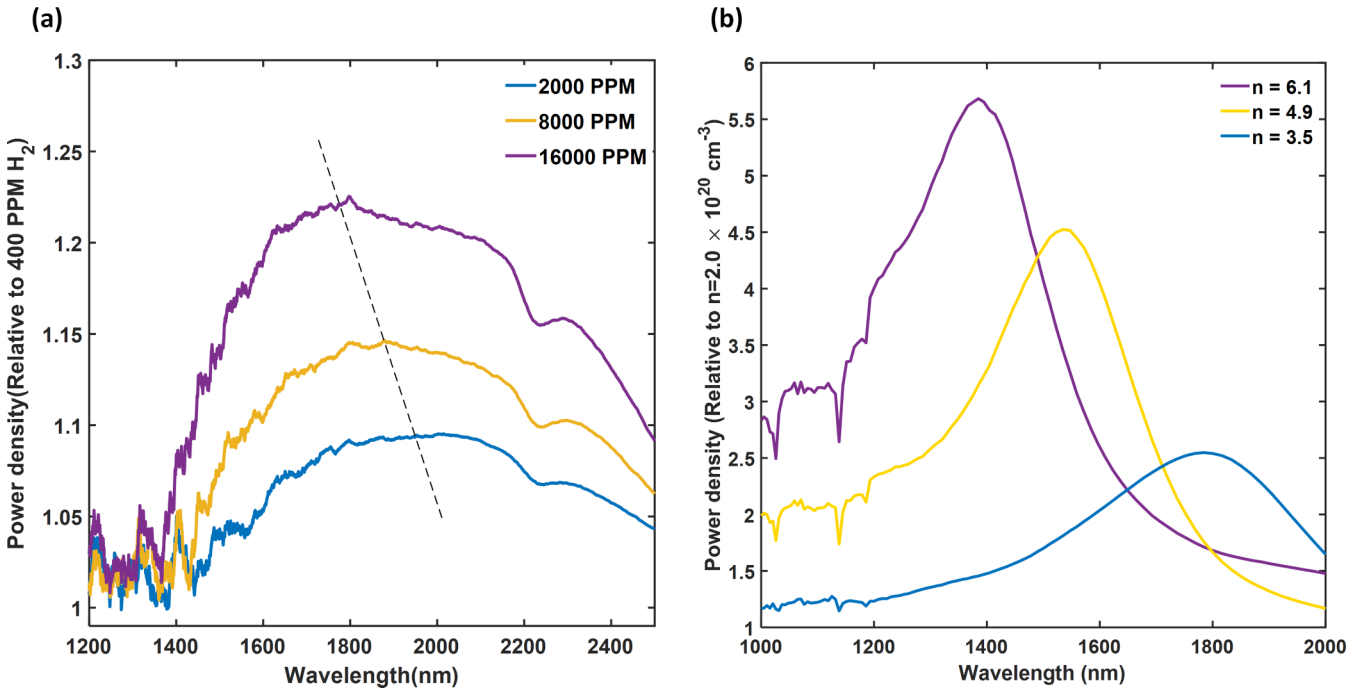

FIG. 4. (a) Power density measured at different H_2 concentrations, where the black dashed line indicates the blueshift of the SPR. The dashed line is a guide for the eyes. (b) Reduced power density relative to the case of ITO film carrier concentration value of $2.0 \times 10^{20}\,\mathrm{cm}^{-3}$, n is in the unit of $10^{20}\,\mathrm{cm}^{-3}$.

the near-field modes can be transferred to the far field. Such thermal extraction can be better appreciated from the reduced power spectrum $\phi(\lambda, T)/\Theta(\omega, T)$, where $\phi(\lambda, T)$ is the measured or calculated power density spectrum and $\Theta(\lambda, T)$ is the Planck distribution term.

As mentioned in the previous section, the optical properties of the ITO thin film are subject to change under different chemical environments. Specifically, the free carrier concentration of the ITO thin film can be strongly altered upon the exposure to H_2 gas at high temperatures. The correlation between the partial H_2 concentration and the ITO thin film free carrier concentration was reported in our previous work [28]. First taking the collected thermal emission of the film under 1% O_2 as a baseline, the fiber is then exposed to H_2 at several concentrations: 400, 2000, 8000, and 16 000 ppm. After 1 hour(h) at each concentration, the thermal emission spectrum is collected. The power density at each concentration, normalized relative to the case of 400 ppm H_2 is shown in Fig. 4(a). Between H_2 exposure steps, 1% O_2 is flowed for 1 h to return the film and fiber to baseline conditions. In Fig. 4(b), the simulation results of reduced radiative heat flux from the ITO thin film to the far field is plotted at different carrier concentrations: 2.0, 3.5, 4.9, and 6.1 (in the unit of $10^{20}\,\mathrm{cm}^{-3}$). The power density at each carrier concentration is normalized to the values at $2.0 \times 10^{20}\,\mathrm{cm}^{-3}$. Strong surface plasmon peaks show up within those curves and a blueshift of resonance wavelength is observed. For carrier concentration of $2.0 \times 10^{20}\,\mathrm{cm}^{-3}$, the resonance lies beyond 2 μm and therefore cannot be seen from the current plot. Although the exact correlation between the ambient H_2 concentration and the ITO film carrier concentration is difficult to obtain, the general trend is revealed as that increasing H_2 concentration leads to higher carrier concentration [34–36]. The experimentally measured power density relative to the 400 ppm H_2 baseline in Fig. 4(a) shows the similar blueshift trend of the plasmon resonance as seen from the simulation results. The broadening of peaks in Fig. 4(a) may be due to the interference of the NIR silica hydroxyl absorption in the fiber, which is not completely normalized. Besides, the imperfections of the sample such as the surface roughness of the film and inhomogeneities at the edge of the etched region could contribute to the distortion or broadening of the ITO film SPR peaks as well.

IV. CONCLUSION

In this work, we experimentally demonstrate the feasibility of using high-index optical waveguides as an efficient thermal extraction device. As an experimental platform, the waveguide coupled thermal extraction technique developed in this work can potentially be used to measure the spectral near-field responses from a variety of materials like thin films and nanostructures. Although the demonstrated near-field thermal emission spectra are mainly in the NIR range, the spectral measurements can be extended to a much broader infrared range by using the waveguides based on infrared transparent materials.

By directly calculating the thermal emission from the ITO thin film coupled with planar optical waveguide using the WCE method, we elucidate the physics of thermal extraction in the emitter-waveguide system. Two times larger thermal emission is extracted from the ITO-waveguide system, and such an enhancement corresponds to several orders of magnitude more heat flux due to the small detector area required in the case of the ITO-waveguide coupled system. The further simulation on the ITO-optical fiber system with a huge aspect

ratio reaches good agreement with the measurement data. The blueshift trend of the plasmon resonance with increasing H_2 concentration is captured in both simulation and experiment. The integration between nanoscale thermal emitter and optical fiber system paves the way for the remote and high-fidelity chemical sensing, infrared imaging, and near-field thermal energy management.

ACKNOWLEDGMENTS

This work was primarily supported by the Defense Threat Reduction Agency (Grant No. HDTRA1-18-1-0046). This work was funded partially by the Dowd Fellowship from the College of Engineering at Carnegie Mellon University. The authors would like to thank Philip and Marsha Dowd for their financial support and encouragement. This work was performed partially under the support of the Crosscutting Research Program under the National Energy Technology Laboratory (NETL) Research & Innovation Center Advanced Sensors and Controls Field Work Proposal. This research was also supported in part by an appointment to the NETL Research Participation Program, sponsored by the U.S. Department of Energy and administered by the Oak Ridge Institute for Science and Education. This report was prepared as an account of work sponsored by an agency of the United States Government. Neither the United States Government nor any agency thereof, nor any of their employees, makes any warranty, express or implied, or assumes any legal liability or responsibility for the accuracy, completeness, or usefulness of any information, apparatus, product, or process disclosed, or represents that its use would not infringe privately owned rights. Reference herein to any specific commercial product, process, or service by trade name, trademark, manufacturer, or otherwise does not necessarily constitute or imply its endorsement, recommendation, or favoring by the United States Government or any agency thereof. The views and opinions of authors expressed herein do not necessarily state or reflect those of the United States Government or any agency thereof.

The manuscript was written through contributions of all authors. All authors have given approval to the final version of the manuscript.

The authors declare no competing financial interest.

APPENDIX: DIRECT SIMULATION AND EXPERIMENTAL MEASUREMENT METHOD OF THERMAL EXTRACTION

Wiener chaos expansion method. According to fluctuational electrodynamics, thermal radiation originates from thermally induced random currents. When we consider a thermal emitter V_E at temperature T, the field intensity $\langle|\boldsymbol{E}(r,\omega)^2|\rangle$ can be expressed in terms of the Dyadic Green's function and random currents $\boldsymbol{j}(r',\omega)$ as

$$\langle|\boldsymbol{E}(r,\omega)^2|\rangle = \omega^2\mu_0^2\Theta(\omega,T)\varepsilon_0\,\mathrm{Im}[\varepsilon]\int dr'^3 \times \int dr''^3\,\mathrm{Tr}[\boldsymbol{G}(r,r',\omega)^*\cdot\boldsymbol{G}(r,r'',\omega) \cdot\langle j(r'',\omega)j(r',\omega)\rangle]. \tag{A1}$$

In order to efficiently evaluate Eq. (A1), the WCE formulation is used to calculate the thermal radiation of arbitrary geometries by expanding the thermally induced random current $\boldsymbol{j}(r',\omega)$ into deterministic orthonormal current modes. As a result, thermal radiative heat flux and field profile are obtained by the sum of the energy flux and the field emitted from each current mode, respectively. According to fluctuational electrodynamics, the second moments of the random currents satisfies that

$$\langle\boldsymbol{j}(r,\omega)\boldsymbol{j}^*(r',\omega)\rangle = V_T(r,\omega)^2\delta(r-r')\boldsymbol{I}, \tag{A2}$$

where $\langle\boldsymbol{j}(r,\omega)\rangle$ is attributed to the unbiased nature of the thermal fluctuation and $V_T(r,\omega)=\sqrt{\frac{4}{\pi}\omega\varepsilon_0\,\mathrm{Im}[\varepsilon(r)]\Theta(\omega,T)}$ is a deterministic quantity. The random current $\boldsymbol{j}(r,\omega)$ can be mathematically constructed as

$$\boldsymbol{j}(r,\omega) = V_T(r,\omega)dW_i(r)\hat{\boldsymbol{i}}, \quad r\in V_E, i=x,y,z, \tag{A3}$$

where dW_x, dW_y and dW_z are the white-noise stochastic processes that have the properties of $\langle dW_l(r)\rangle = 0$, $\langle dW_l(r)\cdot dW_k(r')\rangle = \delta(r-r')$ for $r,r'\in V_E$; $l,k\in\{x,y,z\}$. In addition, dW_x, dW_y, dW_z are independent of each other, i.e., $\langle dW_l(r)\cdot dW_k(r')\rangle = \langle dW_l(r)\cdot dW_k(r)\rangle = 0$ for $l\neq k$; $l,k\in\{x,y,z\}$, indicating that the random polarization of the random current is $\langle\boldsymbol{j}(r,\omega)\rangle$. Such a stochastic process can be expanded onto a deterministic orthonormal basis by the WCE method as [30]

$$dW_m(r) = \sum_{n=1}^{\infty} c_{mn}\cdot f_n(r), \quad r\in V_E, m=x,y,z, \tag{A4}$$

where c_{mn} are the uncorrelated random variables satisfying $\langle c_{ml}\rangle\ \langle c_{ml}\cdot c_{mk}\rangle = \delta_{lk}\cdot\{f_n(r)\}$. $\{f_n(r)\}$ is a set of orthonormal basis functions defined in the volume of the thermal emitter V_E. Therefore, the second moment of random current $\langle\boldsymbol{j}(r,\omega)\boldsymbol{j}^*(r',\omega)\rangle$ in Eqs. (A2) and (A3) can be readily expressed as $\langle\boldsymbol{j}(r,\omega)\boldsymbol{j}^*(r',\omega)\rangle = \sum_n V_T^2 f_n(r)f_n(r')\boldsymbol{I}$. By substituting Eqs.(A2)–(A4) into Eq. (1), thermal radiation field intensity $\langle|\boldsymbol{E}(r,\omega)^2|\rangle$ can be expanded in terms of current modes based on the aforementioned derivation as

$$\langle|\boldsymbol{E}(r,\omega)^2|\rangle = \sum_n\left|E_n^2\right| = \sum_n\{\boldsymbol{L_E}[\boldsymbol{j}_{n,i}\cdot\boldsymbol{j}^*_{n,i}]\}, \quad i=x,y,z, \tag{A5}$$

where the operator $\boldsymbol{L_E}[\cdot]$ is defined as $\boldsymbol{L_E}[X] = \omega^2\mu_0^2\int dr'^3\int dr''^3\,\mathrm{Tr}[\boldsymbol{G}(r,r',\omega)^*\cdot\boldsymbol{G}(r,r'',\omega)\cdot\boldsymbol{X}]$.

In calculating the thermal radiation for the case of ITO-waveguide system, the emitting volume is evaluated in the Cartesian coordinates with $x\in[0,a]$, $y\in[0,b]$, $z\in[0,c]$. The WCE volumetric current density modes are chosen in the form of a Fourier series as $\boldsymbol{j}_{l,m,n}(r,\omega) = V_T\cdot[H_l(x)P_m(y)Q_n(z)]\{\hat{\boldsymbol{x}},\hat{\boldsymbol{y}},\hat{\boldsymbol{z}}\}$, where the fundamental mode is $\boldsymbol{j}_{0,0,0}(r,\omega) = V_T\cdot\frac{1}{\sqrt{abc}}\{\hat{\boldsymbol{x}},\hat{\boldsymbol{y}},\hat{\boldsymbol{z}}\}$, and $H_l(x)=\sqrt{\frac{2}{a}}\cos[\frac{l\pi x}{a}]$, $P_m(y)=\sqrt{\frac{2}{b}}\cos[\frac{m\pi y}{b}]$, $Q_n(z)=\sqrt{\frac{2}{c}}\cos[\frac{n\pi z}{c}]$. l, m, and n denote the order of the WCE current density modes. For the case of ITO coupled with planar waveguide, $l=0$, $m=0$, and $n=0,1,2,3,4,5$. For the case of ITO coupled with optical fiber, $l=0$, $m=0$, and n is set up to be from 0 to 21 to ensure the convergence of the simulation result.

Optical fiber coupled thermal extraction. In our experiment, a 20-nm-thick ITO film is sputtered on a 3-inch-long region of a commercially available multimode optical fiber (Thorlabs FG105LCA), where the cladding has been etched away by immersion in a buffered HF solution, to a final diameter of approximately 95 μm. Thermal emission is collected from one end of the fiber using a Thorlabs optical spectrum analyzer (OSA – model OSA203B), which spectrally resolves the collected light from 1.0 to 2.6 μm. The OSA is calibrated to convert the collected photon counts to power density (units of pW/nm). To determine the impact of the presence of H_2 on the thermal emission of the film, the fiber is heated to 873 K, while flowing 100 sccm of a gas mixture containing 1% O_2 (balance N_2). After stabilizing at this temperature for 4 h, the fiber is exposed to 0.8% H_2 (8000 ppm, 100 sccm, balance N_2) for 1 h, followed by another exposure to 1% O_2 for 1 h. These two steps are repeated two additional times (6 h total), to ensure that the film is relatively stable under H_2 for subsequent steps.

[1] A. P. Raman, M. A. Anoma, L. Zhu, E. Rephaeli, and S. Fan, Nature (London) **515**, 540 (2014).
[2] J. Kou, Z. Jurado, Z. Chen, S. Fan, and A. J. Minnich, ACS Photon. **4**, 626 (2017).
[3] T. Inoue, M. De Zoysa, T. Asano, and S. Noda, Optica **2**, 27 (2015).
[4] C. R. Otey, W.T. Lau, and S. Fan, Phys. Rev. Lett. **104**, 154301 (2010).
[5] B. Liu, Y. Liu, and S. Shen, Phys. Rev. B **90**, 195411 (2014).
[6] B. Yu, J. Li, and S. Shen, J. Photon. Energy **9**, 032712 (2019).
[7] B. Liu, J. Li, and S. Shen, ACS Photon. **4**, 1552 (2017).
[8] J. Li, B. Liu, and S. Shen, Phys. Rev. B **96**, 075413 (2017).
[9] S. Basu, Z. M. Zhang, and C. J. Fu, Int. J. Energy Res. **33**, 1203 (2009).
[10] X. Liu, T. Tyler, T. Starr, A. F. Starr, N. M. Jokerst, and W. J. Padilla, Phys. Rev. Lett. **107**, 045901 (2011).
[11] S. Shin, M. Elzouka, R. Prasher, and R. Chen, Nat. Commun. **10**, 1377 (2019).
[12] A. I. Volokitin and B. N. J. Persson, Rev. Mod. Phys. **79**, 1291 (2007).
[13] K. Joulain, J.-P. Mulet, F. Marquier, R. Carminati, and J.-J. Greffet, Surf. Sci. Rep. **57**, 59 (2005).
[14] M. P. Bernardi, D. Milovich, and M. Francoeur, Nat. Commun. **7**, 12900 (2016).
[15] S. Shen, A. Narayanaswamy, and G. Chen, Nano Lett. **9**, 2909 (2009).
[16] J. Shi, B. Liu, P. Li, L.Y. Ng, and S. Shen, Nano Lett. **15**, 1217 (2015).
[17] E. Rousseau, A. Siria, G. Jourdan, S. Volz, F. Comin, J. Chevrier, and J.-J. Greffet, Nat. Photon. **3**, 514 (2009).
[18] D. Thompson, L. Zhu, R. Mittapally, S. Sadat, Z. Xing, P. McArdle, M. M. Qazilbash, P. Reddy, and E. Meyhofer, Nature (London) **561**, 216 (2018).
[19] A. Fiorino, L. Zhu, D. Thompson, R. Mittapally, P. Reddy, and E. Meyhofer, Nat. Nanotechnol. **13**, 806 (2018).
[20] K. Kim, B. Song, V. Fernández-Hurtado, W. Lee, W. Jeong, L. Cui, D. Thompson, J. Feist, M. T. H. Reid, F. J. García-Vidal, J. C. Cuevas, E. Meyhofer, and P. Reddy, Nature (London) **528**, 387 (2015).
[21] K. Kloppstech, N. Könne, S.-A. Biehs, A.W. Rodriguez, L. Worbes, D. Hellmann, and A. Kittel, Nat. Commun. **8**, 14475 (2017).
[22] M. Lim, J. Song, S. S. Lee, and B. J. Lee, Nat. Commun. **9**, 4302 (2018).
[23] A. Babuty, K. Joulain, P.-O. Chapuis, J.-J. Greffet, and Y. De Wilde, Phys. Rev. Lett. **110**, 146103 (2013).
[24] A. C. Jones and M. B. Raschke, Nano Lett., **12**, 1475 (2012).
[25] Z. Yu, N. P. Sergeant, T. Skauli, G. Zhang, H. Wang, and S. Fan, Nat. Commun. **4**, 1730 (2013).
[26] Y. Tan, B. Liu, S. Shen, and Z. Yu, Nanophotonics **5**, 22 (2016).
[27] B. Liu and S. Shen, Phys. Rev. B **87**, 115403 (2013).
[28] J. L. Poole, Y. Yu, and P. R. Ohodnicki, Sci. Rep. **7**, 9518 (2017).
[29] K. Nishio, T. Sei, and T. Tsuchiya, J. Mater. Sci. **31**, 1761 (1996).
[30] S.-B. Wen, J. Heat Transfer **132**, 072704 (2010).
[31] Z. C. Holman, M. Filipič, A. Descoeudres, S. De Wolf, F. Smole, M. Topič, and C. Ballif, J. Appl. Phys. **113**, 013107 (2013).
[32] See Supplemental Material at http://link.aps.org/supplemental/10.1103/PhysRevB.99.235414 for far-field power collection method, y- and z-component Poynting vector distrbution from ITO and planar waveguide structure, and total far-field thermal emission from ITO-waveguide system under different geometry conditions.
[33] C. S. Kim, I. Vurgaftman, R. A. Flynn, M. Kim, J. R. Lindle, W. W. Bewley, K. Bussmann, J. R. Meyer, and J. P. Long, Opt. Exp. **18**, 10609 (2010).
[34] Y. Jee, Y. Yu, H. W. Abernathy, S. Lee, T. L. Kalapos, G. A. Hackett, and P. R. Ohodnicki, ACS Appl. Mater. Interfaces **10**, 42552 (2018).
[35] P. R. Ohodnicki, C. Wang, and M. Andio, Thin Solid Films **539**, 327 (2013).
[36] P. R. Ohodnicki, M. Andio, and C. Wang, J. Appl. Phys **116**, 24309 (2014).